Optimal Path Following for Small Fixed-Wing UAVs Under Wind Disturbances

Jun Yang, *Senior Member, IEEE*, Cunjia Liu, *Member, IEEE*, Matthew Coombes, Yunda Yan, *Member, IEEE*, and Wen-Hua Chen, *Fellow, IEEE*

***Abstract*— This article presents a novel path-following algorithm for fixed-wing unmanned aerial vehicles by virtue of a nonlinear optimal control approach and wind disturbance observers. Different from some exiting algorithms, the proposed algorithm formulates the path-following problem into a control problem by introducing auxiliary dynamics for the path parameter. The proposed controller is designed in an optimal and systematic manner where the control action is generated according to a well-defined cost function. This framework does not require any complex geometric coordinate transformation and can be easily tuned to accommodate curved reference paths, making it straightforward to deploy in different flight missions. Moreover, the wind influences on the path-following performance is explicitly compensated by the proposed algorithm based on the wind estimates provided by nonlinear disturbance observers. The closed-loop stability, including the auxiliary dynamics for path parameter and observer dynamics for wind estimation, is also analyzed. The feasibility and effectiveness of the proposed algorithm have been thoroughly validated in simulation studies and realistic flight tests.**

***Index Terms*— Disturbance observer, optimal control, path following, unmanned aerial vehicle (UAV).**

I. Introduction

RECENT years have witnessed many successful applications of unmanned aerial vehicles (UAVs) in different domains, ranging from environmental monitoring, search, and rescue to surveillance and reconnaissance. Most of the common UAV tasks require to cruise along a predefined geometric path [1], [2]. This function also forms the basis for more challenging tasks, such as stand-off tracking [3] and moving path following of ground vehicles [4]. Small or miniature fixed-wing UAVs are particularly suitable for these kinds of tasks due to their low costs, long flight range, and endurance. However, the aerodynamic nature of fixed-wing UAVs means that their performance is highly dependent on the environmental wind condition, where the wind can be a significant percentage of UAV's operational airspeed.

Several fundamental studies suggest that path following is a better way to guide a fixed-wing UAV to travel on a predefined geometric path [5]–[7], which does not require the UAV to be a particular location at a prespecified time as in trajectory tracking. This also allows a UAV to fly at a constant airspeed as opposed to a demanded ground speed, providing benefits such as reducing energy consumption, preventing stall in downwind flight, and retaining the UAV dynamics within a linear region [8].

Due to the practicality and significance, the path-following problem has been extensively investigated in various literature works. A survey of some basic path-following functions can be found in [9]. In general, the path-following problem can be solved by exploring the geometric properties of the problem and/or formulating it into a control problem. Popular geometric methods include vector-field techniques [10], [11], which aim to calculate a desired heading for the UAV based on the relative distance from a straight line or circle reference path. Vector-field-based methods are widely used in different applications (see [3], [12]), including recent advances for complicated star curves [13]. To solve the problem of following general curved paths, different approaches based on the virtual target point (VTP) concept have been developed [14], [15]. The Serret–Frenet frame transformation is often employed to properly define the error dynamics between the UAV and the VTP traveling on the reference path so that different control techniques can be applied to stabilize the error dynamics (see [16]–[20]). Advanced control methods can also be directly applied to path-following problems. For example, a nested saturation control approach is presented in [8] to solve the input constraint problem of fixed-wing UAV path following. A linear model predictive control approach is presented in [21] for guidance law design, where the UAV dynamics are linearized around certain operation points. Nonlinear model predictive control methods have also been seen in tackling path-following problems [22], [23].

In spite of extensive results on UAV path-following problems, there is still room to improve the algorithm's

Manuscript received May 5, 2019; revised February 29, 2020; accepted March 4, 2020. Date of publication April 21, 2020; date of current version April 12, 2021. Manuscript received in final form March 9, 2020. This work was supported in part by the U.K. Engineering and Physical Science Research Council (EPSRC) under Grant EP/P012868/1, in part by the National Natural Science Foundation of China (NSFC) under Grant 61973080, and in part by the Shenzhen Science and Technology Plan under Grant JCYJ20190813152603594. The research data supporting this publication have been provided within the paper. The raw flight test data can be found at https://doi.org/10.17028/rd.lboro.12124131. Recommended by Associate Editor A. Serrani. *(Corresponding author: Cunjia Liu.)*

Jun Yang is with the School of Automation, Southeast University, Nanjing 210096, China, and also with the Department of Aeronautical and Automotive Engineering, Loughborough University, Loughborough LE11 3TU, U.K. (e-mail: j.yang84@seu.edu.cn).

Cunjia Liu, Matthew Coombes, Yunda Yan, and Wen-Hua Chen are with the Department of Aeronautical and Automotive Engineering, Loughborough University, Loughborough LE11 3TU, U.K. (e-mail: c.liu5@lboro.ac.uk; m.j.coombes@lboro.ac.uk; yd.yan@ieee.org; w.chen@lboro.ac.uk).

This article has supplementary downloadable material available at https://ieeexplore.ieee.org, provided by the authors.

Color versions of one or more of the figures in this article are available online at https://ieeexplore.ieee.org.

Digital Object Identifier 10.1109/TCST.2020.2980727

performance and practicability. The geometric methods designed for curved paths usually involve complicated frame transformation, which may also pose requirements on how to design and parameterize the reference path. Moreover, the evolutionary law of the geometric path parameter is often designed and tuned separately from the control law for UAV kinematics. As such, the path parameter law may not be produced in an optimized way to ensure a coherent path-following performance. The objective of this article is, thus, to develop a simple and lightweight path-following algorithm suitable for low-cost autopilots on many small UAVs to improve their path-following capability.

Inspired by a recent work [24], we present a novel optimal path-following algorithm for small fixed-wing UAVs to follow 3-D curves. An auxiliary dynamics for the path parameter is introduced and the corresponding virtual control input is produced by solving the integrated optimization problem. Different from [24], this article utilizes an explicit nonlinear optimal control design. The proposed controller provides an analytic solution without any online optimization computation, which gives an intuitive way for implementation. In addition, the path-following errors are regulated in an optimal manner, which ensures better path-following performance. The guideline for tuning the weighting matrices and the prediction horizon associated with the proposed algorithm are discussed in detail, which is also related to asymptomatic stability of the closed-loop systems.

Another problem to be addressed in path following of fixed-wing UAV is the influence of environmental wind, which can cause significant discrepancy between the wind frame, where the UAV is operated, and the ground framework, where the reference path is defined. A commonly adopted approach is to use ground speed and course angle for path-following algorithm design [10]. However, in practice, the ground speed and course from a low-cost GPS module may be degraded, affecting the overall system performance, which also suggests that more attention should be paid to airspeed measurement and magnetic heading. Recently, more works have explicitly considered the wind velocity in their algorithm designs (see [8], [22]), where the wind velocities are assumed to be known to the algorithm. Although the existing techniques, such as Kalman filters, may provide a reasonably good wind estimate based on onboard sensors, there still lacks a performance analysis on the overarching system. Another viable solution is to estimate the wind disturbances online and compensate for their influences on the system within the control loop. In [25], an adaptive backstepping control law is proposed to estimate the parameters of the unknown wind disturbances for path following. However, the algorithm is only developed for simple straight lines. A nonlinear disturbance observer is developed in [17] to estimate and then compensate for the undesirable wind under the framework of the Serret–Frenet transformation via the VTP approach, thus being able to deal with curved paths but not in an optimal way.

To overcome the wind disturbance for the proposed optimal path-following algorithm, this article advocates a new disturbance observer-based method. The observers are designed by virtue of higher order sliding mode techniques to provide both velocity and acceleration estimates. These estimates are integrated into prediction and receding horizon optimization processes of the path-following function, which results in an optimized offset-free path-following algorithm for fixed-wing UAVs. Moreover, due to the characteristic of slide mode observer, finite-time estimation can be achieved for any bounded disturbances, which is more suitable for unknown time-varying wind gusts.

To validate the proposed optimal path-following algorithm for windy conditions, comprehensive flight tests have been carried out using a small UAV platform. The results show that the proposed algorithm exhibits promising performance compared with several existing solutions for path following under wind disturbances. It should be mentioned that a preliminary version of the algorithm appeared in [26]. However, the work in [26] did not consider the environmental wind attenuation, did not account for longitudinal controller design, and did not include performance comparison as well as experimental flight tests, all of which are included in this article.

The remainder of this article is organized as follows. The problem formulation, including the kinematic motion for a fixed-wing UAV and the definition of path-following problem, is provided in Section II. The optimal path-following algorithm is derived in Section III, together with the analytic solution to the optimization problem. The disturbance observer-based wind compensation, as well as the closed-loop stability analysis, is given in Section IV. The simulation studies and flight test results are presented in Sections V and VI, respectively, following some concluding remarks in Section VII.

II. Problem Formulation

This article aims to develop an optimal path-following solution for fixed-wing UAVs in wind. The kinematic equations of motion for a generic fixed-wing UAV can be described as [8]

$$\begin{cases} \dot{x} = V\cos\psi\cos\gamma + w_x \\ \dot{y} = V\sin\psi\cos\gamma + w_y \\ \dot{z} = V\sin\gamma + w_z \\ \dot{\psi} = \dfrac{g}{V}\tan\phi_c \\ \dot{\gamma} = \alpha(\gamma_c - \gamma) \end{cases} \tag{1}$$

where x, y, and z denote the 3-D position of the UAV in the inertial frame, V represents the airspeed of the UAV, ψ is the heading angle, and γ denotes the air-relative flight path angle. The inputs to the kinematic model are selected as ϕ_c and γ_c, representing the commanded roll angle and commanded flight path angle, respectively. Note that we follow the coordinated turn assumption [1], [8] to establish the motion for the heading angle ψ. A first-order system with a small time constant α is used to describe the pitch dynamics to accommodate the relatively slow response set up by the inner loop autopilot. The symbols w_x, w_y, and w_z represent the velocity of external wind disturbance along x-, y- and z-axes, respectively.

Since the wind disturbances have been captured in the UAV kinematic model, they will be explicitly dealt with in the proposed path-following framework. An alternative method to circumvent this problem is to use the UAV model based

on ground-referenced measurements (i.e., using course and ground speed instead of heading and airspeed of the UAV), which has been found in many pioneering works (see [10]). The proposed path-following algorithm can also be adapted to this ground-referenced model, although this means that useful information from the airspeed sensor and compass will be discarded and the ground speed from a possibly low-cost GPS module needs to be directly fed into the controller.

The task for the UAV is to follow a desired geometric path in the output space of the model (1). The path can be defined as

$$\begin{aligned}\mathcal{P} \;=\; & \{x, y, z \in \mathbb{R} | \theta \in [\underline{\theta}, \overline{\theta}] \\ & \mapsto x = x_d(\theta), y = y_d(\theta), z = z_d(\theta)\}\end{aligned} \tag{2}$$

where θ is the path parameter and $\underline{\theta}$ and $\overline{\theta}$ denote the minimum and maximum values of the path parameter θ, respectively. Let $\theta_1 = \theta$ and $\theta_2 = \dot{\theta}$. Inspired by [24], the path-following problem can be transferred to a tracking control problem by designing an auxiliary dynamics for the path parameter θ such that

$$\begin{cases} \dot{x} = V\cos\psi\cos\gamma + w_x \\ \dot{y} = V\sin\psi\cos\gamma + w_y \\ \dot{z} = V\sin\gamma + w_z \\ \dot{\psi} = \dfrac{g}{V}\tan\phi_c \\ \dot{\gamma} = \alpha(\gamma_c - \gamma) \\ \dot{\theta}_1 = \theta_2 \\ \dot{\theta}_2 = \mu \end{cases} \tag{3}$$

where μ represents a virtual control law generating the path reference to be followed. Denote $e_x = x - x_d(\theta)$, $e_y = y - y_d(\theta)$, and $e_z = z - z_d(\theta)$ the path-following errors along x-, y-, and z-axes, respectively. It can be seen that in this formulation, only the position of the reference path $\mathcal{P}$ is required and the path parameter θ can be any physical quantity, not necessarily to be the curve length.

The objective of this article is to design the desired control actions ϕ_c, γ_c, and μ such that the path-following errors can converge to zero asymptotically (this means that $x(t) \to x_d(\theta(t))$, $y(t) \to y_d(\theta(t))$, and $z(t) \to z_d(\theta(t))$ as $t \to \infty$) even in the presence of wind disturbances by means of prediction-based optimal control and disturbance estimation-based active compensation.

III. Optimal Path-Following Control

This section details the development of the optimal path-following control algorithm. For the sake of simplification, we use $\omega = g/V\tan\phi_c$ and $\nu = \alpha(\gamma_c - \gamma)$ in the following derivations. Once ω and ν has been obtained, it is straightforward to calculate the implementable control laws as $\phi_c = \arctan(V\omega/g)$ and $\gamma_c = \gamma + (\nu/\alpha)$, respectively.

Let $x = [x, y, z, \psi, \gamma, \theta_1, \theta_2]^T \in \mathbb{R}^7$, $u = [\omega, \nu, \mu]^T \in \mathbb{R}^3$, $d = [w_x, w_y, w_z]^T \in \mathbb{R}^3$, and $e = [e_x, e_y, e_z]^T \in \mathbb{R}^3$ denote the system state, control input, wind disturbance, and path-following error vector, respectively. The dynamics of system (3) can be described by the following compact form:

$$\begin{aligned} \dot{x} &= f(x) + Gu + Pd \\ e &= h(x) \end{aligned} \tag{4}$$

where

$$f(x) = \begin{bmatrix} V\cos\psi\cos\gamma \\ V\sin\psi\cos\gamma \\ V\sin\gamma \\ 0 \\ 0 \\ \theta_2 \\ 0 \end{bmatrix}, \quad G = \begin{bmatrix} 0 & 0 & 0 \\ 0 & 0 & 0 \\ 0 & 0 & 0 \\ 1 & 0 & 0 \\ 0 & 1 & 0 \\ 0 & 0 & 0 \\ 0 & 0 & 1 \end{bmatrix}$$

$$P = \begin{bmatrix} I_{3\times 3} \\ 0_{4\times 3} \end{bmatrix}, \quad h(x) = \begin{bmatrix} h_x(x) \\ h_y(x) \\ h_z(x) \end{bmatrix} = \begin{bmatrix} x - x_d(\theta) \\ y - y_d(\theta) \\ z - z_d(\theta) \end{bmatrix}.$$

Based on this system, we will first derive the optimal path-following control based on the hypothesis that the wind information is available. Then, a practically implementable version of the algorithm will be developed in Section IV using wind disturbance observers, where rigorous stability analysis on the overall closed-loop system will also be provided.

A. Path-Following Error Prediction

To begin with, a cost function of the output path-following problem for the fixed-wing UAV (3) is constructed as

$$J(t) = \left\|\bar{e}(t + T_p)\right\|_P^2 + \int_0^{T_P} \|\bar{e}(t+\tau)\|_Q^2 \, d\tau \tag{5}$$

where T_P is the prediction horizon, P and Q are the terminal and process weighting matrices, respectively, which are symmetric and positive definite, and $\bar{e}(t) = [\bar{e}_x(t), \bar{e}_y(t), \bar{e}_z(t)]^T$ is the predicted output path-following error vector.

The future output path-following error $\bar{e}_\star(t+\tau)$ (for $\star \in \{x, y, z\}$) in the moving horizon is approximated by a Taylor series expansion such that

$$\bar{e}_\star(t+\tau) = e_\star(t) + \tau e_\star^{(1)}(t) + \cdots + \frac{\tau^{2+r}}{(2+r)!} e_\star^{(2+r)}(t) \tag{6}$$

where r is the control order to be assigned as a tuning parameter [27]. As a consequence, the time derivatives of $e_\star(t)$ are calculated and represented as

$$\dot{e}_\star = L_f h_\star(x) + L_P h_\star(x) d \tag{7}$$

where $L_f h_\star(x) := (\partial h_\star(x)/\partial x) f(x)$ and $L_P h_\star(x) := (\partial h_\star(x)/\partial x) P$ are the standard Lie derivatives [28]. Note that for the given specific dynamic system (4), with several intuitive calculations, we have

$$\nabla_x (L_P h_\star(x)) = 0, \;\; L_P L_r h_\star(x) d = 0.$$

where $\nabla_x(b) := (\partial b/\partial x)$ is the standard partial differentiation calculus. Differentiating (7) with respect to time yields

$$\ddot{e}_\star = L_f^2 h_\star(x) + L_G L_f h_\star(x) u + L_P h_\star(x) \dot{d}. \tag{8}$$

Continuously taking derivative of (8) gives

$$e_\star^{(3)} = L_f^3 h_\star(x) + L_G L_f h_\star(x) \dot{u} + p_\star^1(\cdot) \tag{9}$$

where $p_\star^1(\cdot)$ is a function in terms of x, u, d, $\dot{d}$, and $\ddot{d}$, which is given by

$$p_\star^1(\cdot) = L_G L_f h_\star(x)u + L_P L_f^2 h_\star(x)d + L_P h_\star(x)\ddot{d} + \frac{dL_G L_f h_\star(x)}{dt}u + \frac{dL_P h_\star(x)}{dt}\dot{d}.$$

Similarly, the higher order derivatives of $e_\star(t)$ can be calculated and given by

$$e_\star^{(2+k)} = L_f^{2+k} h_\star(x) + L_G L_f h_\star(x) u^{(k)} + p_\star^k(\cdot) \tag{10}$$

for $k = 2, \ldots, r$, where the function $p_\star^k(\cdot)$ is with respect to the arguments of x, $u, \ldots, u^{(k-1)}$, and $d, \ldots, d^{(k+1)}$.

The predictive output path-following error $\bar{e}(t+\tau)$ is defined as

$$\bar{e}(t+\tau) = \begin{bmatrix} \bar{e}_x(t+\tau) \\ \bar{e}_y(t+\tau) \\ \bar{e}_z(t+\tau) \end{bmatrix} = \begin{bmatrix} \bar{\mathcal{T}}, & \tilde{\mathcal{T}} \end{bmatrix} \begin{bmatrix} \bar{Y} \\ \tilde{Y} \end{bmatrix} \tag{11}$$

where

$$\bar{\mathcal{T}}(\tau) = \begin{bmatrix} 1 & \tau & 0 & 0 & 0 & 0 \\ 0 & 0 & 1 & \tau & 0 & 0 \\ 0 & 0 & 0 & 0 & 1 & \tau \end{bmatrix}$$

$$\tilde{\mathcal{T}}(\tau) = \begin{bmatrix} \tilde{\tau}_1 & \cdots & \tilde{\tau}_{r+1} \end{bmatrix}$$

$$\tilde{Y} = \begin{bmatrix} \tilde{Y}_1 \\ \vdots \\ \tilde{Y}_{r+1} \end{bmatrix}, \quad \bar{Y} = \begin{bmatrix} e_x \\ \dot{e}_x \\ e_y \\ \dot{e}_y \\ e_z \\ \dot{e}_z \end{bmatrix}$$

with $\tilde{\tau}_i = (\tau^{i+1}/(i+1)!) I_{3\times 3}$ and $\tilde{Y}_i = [e_x^{(i+1)}, e_y^{(i+1)}, e_z^{(i+1)}]^T$ for $i = 1, \ldots, r+1$.

B. Receding Horizon Optimization

Note that $\bar{Y}$ and $\tilde{Y}$ are independent of τ. The performance index (5) is then rewritten as

$$\begin{aligned} J(t) &= \begin{bmatrix} \bar{Y}^T, \tilde{Y}^T \end{bmatrix} \begin{bmatrix} \bar{\mathcal{T}}(T_p)^T \\ \tilde{\mathcal{T}}(T_p)^T \end{bmatrix} P \begin{bmatrix} \bar{\mathcal{T}}(T_p), & \tilde{\mathcal{T}}(T_p) \end{bmatrix} \begin{bmatrix} \bar{Y} \\ \tilde{Y} \end{bmatrix} \\ &\quad + \int_0^{T_P} \begin{bmatrix} \bar{Y}^T, \tilde{Y}^T \end{bmatrix} \begin{bmatrix} \bar{\mathcal{T}}^T \\ \tilde{\mathcal{T}}^T \end{bmatrix} Q \begin{bmatrix} \bar{\mathcal{T}}, & \tilde{\mathcal{T}} \end{bmatrix} \begin{bmatrix} \bar{Y} \\ \tilde{Y} \end{bmatrix} d\tau \\ &= \begin{bmatrix} \bar{Y}^T, \tilde{Y}^T \end{bmatrix} \begin{bmatrix} \mathcal{T}_1 & \mathcal{T}_2 \\ \mathcal{T}_2^T & \mathcal{T}_3 \end{bmatrix} \begin{bmatrix} \bar{Y} \\ \tilde{Y} \end{bmatrix} \end{aligned} \tag{12}$$

where

$$\mathcal{T}_1 = \bar{\mathcal{T}}(T_p)^T P \bar{\mathcal{T}}(T_p) + \int_0^{T_P} \bar{\mathcal{T}}^T Q \bar{\mathcal{T}} d\tau$$

$$\mathcal{T}_2 = \bar{\mathcal{T}}(T_p)^T P \tilde{\mathcal{T}}(T_p) + \int_0^{T_P} \bar{\mathcal{T}}^T Q \tilde{\mathcal{T}} d\tau$$

$$\mathcal{T}_3 = \tilde{\mathcal{T}}(T_p)^T P \tilde{\mathcal{T}}(T_p) + \int_0^{T_P} \tilde{\mathcal{T}}^T Q \tilde{\mathcal{T}} d\tau.$$

Let $\bar{u} = [u^T, \dot{u}^T, \ldots, (u^{(r)})^T]$. Then, one obtains

$$\frac{1}{2}\frac{\partial J}{\partial \bar{u}} = \left(\frac{\partial \tilde{Y}}{\partial \bar{u}}\right)^T \mathcal{T}_2^T \bar{Y} + \left(\frac{\partial \tilde{Y}}{\partial \bar{u}}\right)^T \mathcal{T}_3 \tilde{Y}. \tag{13}$$

It can be verified that $\partial \tilde{Y}/\partial \bar{u}$ is nonsingular. Letting $\partial J/\partial \bar{u} = 0$, one obtains

$$\tilde{Y} = -\mathcal{T}_3^{-1} \mathcal{T}_2^T \bar{Y}. \tag{14}$$

The first three rows of (14) are written as

$$\tilde{Y}_1 = -K\bar{Y} \tag{15}$$

where K is the first three rows of the matrix $\mathcal{T}_3^{-1}\mathcal{T}_2^T$. The nonlinear receding horizon optimized control law is solved from (15), which is given by

$$u^*(t) = A^{-1}(x)\left[-K\bar{Y} - B(x)\right] \tag{16}$$

where

$$A(x) = \begin{bmatrix} L_G L_f h_x(x) \\ L_G L_f h_y(x) \\ L_G L_f h_z(x) \end{bmatrix}$$

$$B(x) = \begin{bmatrix} L_f^2 h_x(x) + L_P h_x(x)\dot{d} \\ L_f^2 h_y(x) + L_P h_y(x)\dot{d} \\ L_f^2 h_z(x) + L_P h_z(x)\dot{d} \end{bmatrix}$$

$$\bar{Y} = [h_x, L_f h_x + L_P h_x d \quad h_y, L_f h_y + L_P h_y d \quad h_z, L_f h_z + L_P h_z d]^T.$$

With intuitive calculations of $\mathcal{T}_3^{-1}\mathcal{T}_2^T$, it can be obtained that the optimized control gain K has the following form:

$$K = \begin{bmatrix} k_0^x & k_1^x & 0 & 0 & 0 & 0 \\ 0 & 0 & k_0^y & k_1^y & 0 & 0 \\ 0 & 0 & 0 & 0 & k_0^z & k_1^z \end{bmatrix}$$

where the parameters $k_j^\star$ ($\star \in \{x, y, z\}$; $j = 0, 1$) are determined by the predictive period T_P and control order r.

Theorem 1: For the full 3-D motion dynamics (1) of a generic fixed-wing UAV, the proposed optimized path-following algorithm (16) ensures that the path-following errors asymptotically converge to zero, provided that for the given weighting matrices P and Q, there exists the control order $r \in \mathbb{N}$ and the predictive horizon $T_P > 0$ such that polynomials $p_\star(s) = s^2 + k_1^\star s + k_0^\star$ (for $\star \in \{x, y, z\}$) are all Hurwitz.

Proof: Collecting the error dynamics of each output path tracking error given in (8), the full dimensional error dynamics are given by

$$\begin{bmatrix} \ddot{e}_x \\ \ddot{e}_y \\ \ddot{e}_z \end{bmatrix} = \begin{bmatrix} L_f^2 h_x + L_P h_x \dot{d} \\ L_f^2 h_y + L_P h_y \dot{d} \\ L_f^2 h_z + L_P h_z \dot{d} \end{bmatrix} + \begin{bmatrix} L_G L_f h_x \\ L_G L_f h_y \\ L_G L_f h_z \end{bmatrix} u. \tag{17}$$

Substituting the optimal control law (16) into (17), the dynamic closed-loop system is then governed by

$$\ddot{e}_\star + k_1^\star \dot{e}_\star + k_0^\star e_\star = 0 \tag{18}$$

(for $\star \in \{x, y, z\}$). Consequently, the following matrix:

$$A_\star = \begin{bmatrix} 0 & 1 \\ -k_0^\star & -k_1^\star \end{bmatrix} \tag{19}$$

is Hurwitz, which indicates that the error dynamics in (18) are asymptotically stable. This completes the proof of Theorem 1 ■

In practice, the stability can be easily verified after the controller parameters are selected. Moreover, by introducing the extra terminal cost with the weighting matrix P to the standard cost function used in [27], more tuning flexibility has been introduced for the first time to this kind of algorithms, allowing the control gains (or the convergence rate) in different channels to be adjusted independently for a multiple-input–multiple-output system. It is also assumed that the internal zero dynamics of the system is stable, which can be verified in simulations and experiments.

IV. Practical Path Following Using Wind Disturbance Observers

As mentioned in Section III, the wind information should be utilized for disturbance compensation for the proposed optimal path-following algorithm. For the purpose of practical implementation, it would be imperative to design observers to estimate the velocity as well as acceleration of the wind gusts. In this section, we aim to develop wind gust observers to assist disturbance estimation and compensation.

A. Design of Wind Disturbance Observers

First, the observer to estimate w_x and $\dot{w}_x$ is designed as

$$\begin{cases} \dot{\hat{x}} = V\cos\psi\cos\gamma + \hat{w}_x + l_{x1}L_x^{\frac{1}{3}}\lfloor x-\hat{x}\rceil^{\frac{2}{3}} \\ \dot{\hat{w}}_x = \hat{a}_x + l_{x2}L_x^{\frac{1}{2}}\lfloor x-\hat{x}\rceil^{\frac{1}{2}} \\ \dot{\hat{a}}_x = l_{x3}L_x\text{sign}(x-\hat{x}) \end{cases} \tag{20}$$

where $\hat{x}$, $\hat{w}_x$, and $\hat{a}_x$ denote the estimates of x, w_x, and $a_x = \dot{w}_x$, respectively. Define the observer errors as $\epsilon_x = x - \hat{x}$, $\epsilon_{wx} = w_x - \hat{w}_x$, and $\epsilon_{ax} = a_x - \hat{a}_x$. The estimation error dynamics are given by

$$\begin{cases} \dot{\epsilon}_x = \epsilon_{wx} - l_{x1}L_x^{\frac{1}{3}}\lfloor\epsilon_x\rceil^{\frac{2}{3}} \\ \dot{\epsilon}_{wx} = \epsilon_{ax} - l_{x2}L_x^{\frac{1}{2}}\lfloor\epsilon_x\rceil^{\frac{1}{2}} \\ \dot{\epsilon}_{ax} = \dot{a}_x - l_{x3}L_x\text{sign}(\epsilon_x). \end{cases} \tag{21}$$

It has been shown in [29] that the error dynamics (21) is finite-time stable if the observer scaler gain is designed such that $L_x > \dot{a}_x$. In a similar manner, the wind disturbance observers for y-frame and z-frame are designed as follows:

$$\begin{cases} \dot{\hat{y}} = V\sin\psi\cos\gamma + \hat{w}_y + l_{y1}L_y^{\frac{1}{3}}\lfloor y-\hat{y}\rceil^{\frac{2}{3}} \\ \dot{\hat{w}}_y = \hat{a}_y + l_{y2}L_y^{\frac{1}{2}}\lfloor y-\hat{y}\rceil^{\frac{1}{2}} \\ \dot{\hat{a}}_y = l_{y3}L_y\text{sign}(y-\hat{y}) \end{cases} \tag{22}$$

where $\hat{y}$, $\hat{w}_y$, and $\hat{a}_y$ denote the estimates of y, w_y, and $a_y = \dot{w}_y$, respectively, and

$$\begin{cases} \dot{\hat{z}} = V\sin\gamma + \hat{w}_z + l_{z1}L_z^{\frac{1}{3}}\lfloor z-\hat{z}\rceil^{\frac{2}{3}} \\ \dot{\hat{w}}_z = \hat{a}_z + l_{z2}L_z^{\frac{1}{2}}\lfloor z-\hat{z}\rceil^{\frac{1}{2}} \\ \dot{\hat{a}}_z = l_{z3}L_z\text{sign}(z-\hat{z}) \end{cases} \tag{23}$$

where $\hat{z}$, $\hat{w}_z$, and $\hat{a}_z$ denote the estimates of z, w_z, and $a_z = \dot{w}_z$, respectively. Similar to the observer error dynamics (21), it can be shown that the finite-time stability of the abovementioned two wind disturbance observers (22) and (23) is guaranteed if the observer scalar gains are assigned such that $L_y > \dot{a}_y$ and $L_z > \dot{a}_z$ [29]. This indicates that after the transient process of convergence of the errors, one has that $w_\star = \hat{w}_\star$ and $\dot{w}_\star = a_\star = \hat{a}_\star$ (for $\star \in \{x, y, z\}$).

It should be noted that for the conventional nonlinear observers, asymptotic or finite-time convergence only can be achieved on the assumption that the external disturbance is constant or generated by an exosystem (see [30], [31]). In the case where nonvanishing model error exists in the exosystem, only input-to-state stability (ISS) can be achieved, which may be not suitable for high-precision path following under unknown time-varying wind. This motivates the use of sliding mode observers. Due to the characteristic of sliding mode, finite-time estimation can be achieved for any bounded disturbances.

B. Practical Path-Following Algorithm

By replacing the unknown inputs d and $\dot{d}$ in (24) with their estimates $\hat{d}$ and $\hat{a}$ generated by wind disturbance observers, the practically implementable path-following algorithm is designed and given by:

$$u(t) = -A^{-1}(x)v(x, \hat{d}, \hat{a}) \tag{24}$$

where $v(\cdot) = [v_x(\cdot), v_y(\cdot), v_z(\cdot)]^T$ with

$$v_\star(x, \hat{d}, \hat{a}) = k_0^\star h_x(x) + k_1^\star(L_f h_\star(x) + L_P h_\star(x)\hat{d}) + L_f^2 h_\star(x) + L_P h_\star(x)\hat{a}.$$

The implementable control laws of the proposed path-following algorithm is calculated in detail in the Appendix.

Substituting the proposed optimized offset-free path-following algorithm (24) into the open-loop path-following error dynamics (17), the dynamic closed-loop system is then governed by

$$\ddot{e}_\star + k_1^\star\dot{e}_\star + k_0^\star e_\star = k_1^\star L_P h_\star(x)\tilde{d} + L_P h_\star(x)\tilde{a} \tag{25}$$

where $\tilde{d}$ and $\tilde{a}$ denote the observation errors of wind gust disturbances defined by

$$\tilde{d} = d - \hat{d}, \quad \tilde{a} = \dot{d} - \hat{a}.$$

Theorem 2: For the full 3-D motion dynamics (1) of a generic fixed-wing UAV, the proposed composite path-following algorithm (24) with wind disturbance observers (20), (22), and (23) ensures that the path-following errors asymptotically converge to zero, provided that for the given weighting matrices P and Q, there exists the control order $r \in \mathbb{N}$ and the predictive horizon $T_P > 0$ such that polynomials $p_\star(s) = s^2 + k_1^\star s + k_0^\star$ (for $\star \in \{x, y, z\}$) are all Hurwitz and the observer scalar gains are chosen as $L_\star > \dot{a}_\star$.

Proof: The proof of the theorem is divided into two steps as follows. In the first step, we will show that the path-following errors are ultimately bounded under the given conditions. Thereafter, it will be shown that the tracking errors under the practical path-following algorithm converge to zero asymptotically.

Step 1: As the wind disturbance observers (20), (22), and (23) are finite-time stable, one has

$$\begin{aligned} \|\tilde{d}(t)\| \le \bar{d}, \quad \|\tilde{a}(t)\| \le \bar{a}, \ \text{for } t \in [0,\infty) \\ \tilde{d}(t) = 0, \quad \tilde{a}(t) = 0, \ \text{for } t \ge T_1 \end{aligned} \tag{26}$$

where $\bar{d}$ and $\bar{a}$ are positive constants, and T_1 is a finite time covering the convergence process of the observer dynamics. With straightforward calculations, we can obtain that $L_P h_\star(x)$ is a constant vector independent of the argument x, which indicates that

$$\|L_P h_\star(x)\| \le \bar{m}_\star \ \forall x \in \mathbb{R}^7. \tag{27}$$

Since $A_\star$ in (19) is a Hurwitz matrix, one obtains that there exists a positive-definite matrix $P_\star$ such that

$$A_\star^T P_\star + P_\star A_\star = -2I_{2\times 2}. \tag{28}$$

Let $e_\star = [e_\star, \dot{e}_\star]^T$ and define a candidate Lyapunov function as $V_\star(e_\star) = \frac{1}{2} e_\star^T P_\star e_\star$. The maximum and minimum eigenvalues of $A_\star$ are defined as $\lambda_{\max}(A_\star)$ and $\lambda_{\min}(A_\star)$, respectively. With (28) in mind, taking derivative of $V_\star(e_\star)$ along (25) gives

$$\begin{aligned} \dot{V}_\star(e_\star) &= -\|e_\star\|^2 + e_\star^T P_\star \begin{bmatrix} 0 \\ k_1^\star L_P h_\star(x)\tilde{d} + L_P h_\star(x)\tilde{a} \end{bmatrix} \\ &\le -\|e_\star\|^2 + \|e_\star\| \cdot \|P_\star\| \left(k_1^\star \bar{m}_\star \bar{d} + \bar{m}_\star \bar{a}\right) \\ &\le -\alpha_\star V_\star(e_\star) + \beta_\star \end{aligned} \tag{29}$$

with $\alpha_\star = 1/\lambda_{\max}(A_\star)$ and $\beta_\star = \|P_\star\|^2 (k_1^\star \bar{m}_\star \bar{d} + \bar{m}_\star \bar{a})^2$. Using the comparison lemma [32], it further follows from (28) and (29) that:

$$\begin{aligned} \|e_\star(t)\|^2 &\le \frac{2}{\lambda_{\min}(A_\star)} \left[V_\star(0) e^{-\alpha_\star t} + \frac{\beta_\star}{\alpha_\star}(1 - e^{-\alpha_\star t}) \right] \\ &\le -\bar{\alpha}_\star e^{-\alpha_\star t} + \bar{\beta}_\star \end{aligned} \tag{30}$$

with

$$\bar{\alpha}_\star = \frac{\lambda_{\max}(A_\star)}{\lambda_{\min}(A_\star)} \|e_\star(0)\|^2 - \frac{2\beta_\star}{\lambda_{\min}(A_\star)\alpha_\star}, \ \bar{\beta}_\star = \frac{2\beta_\star}{\lambda_{\min}(A_\star)\alpha_\star}.$$

The ultimately boundedness property of the path-following errors then directly follows from (30).

Step 2: Since the path-following errors are ultimately bounded, we can consider the stability and convergence of the errors for the time interval $t \in [T_1, \infty)$. It has been shown in (26) that $\tilde{d}(t) = 0$ and $\tilde{a}(t) = 0 \ \forall t \ge T_1$. As a consequence, in the time interval $t \in [T_1, \infty)$, the path-following errors in (25) reduce to:

$$\ddot{e}_\star + k_1^\star \dot{e}_\star + k_0^\star e_\star = 0 \tag{31}$$

which is asymptotically stable. This completes the proof of Theorem 2. ■

V. Simulation Studies

Numerical simulations were carried out to demonstrate the performance and parameter tuning of the proposed algorithm in following 3-D curves. As mentioned in Section I, the proposed algorithm can be used for more general geometric paths in addition to circle and straight-line paths. Hence, a bow-tie-shaped path is designed as the reference to be followed, whose mathematical expression is given by

$$\begin{bmatrix} x_d(\theta) \\ y_d(\theta) \\ z_d(\theta) \end{bmatrix} = \begin{bmatrix} 150\cos\theta \\ 75\sin(2\theta) \\ 200 + 30\cos\theta \end{bmatrix} \text{m}.$$

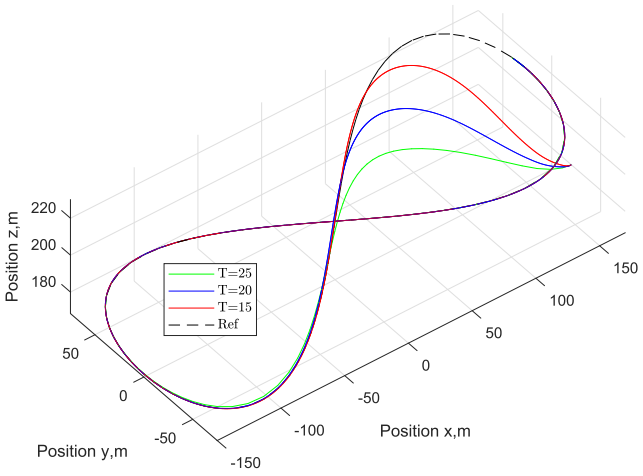

Fig. 1. Position profiles of a "bow-tie"-shaped path-following simulation for a fixed-wing UAV in the presence of wind gusts under different prediction horizons T_p.

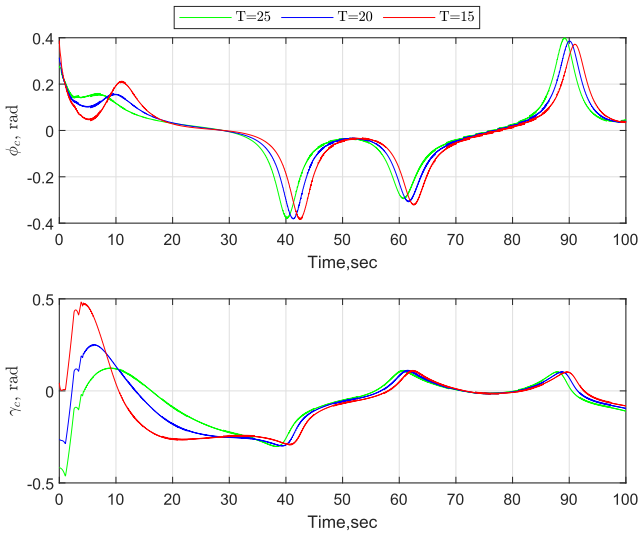

Fig. 2. Corresponding control inputs of a "bow-tie"-shaped path-following simulation under different prediction horizons T_p.

A. Discussion on the Effects of the Prediction Horizon T_p

The controller and observer parameters of the proposed approach are designed as $r = 1$, $P = 0_{3\times 3}$, $Q = I_{3\times 3}$, $l_{x1} = l_{y1} = l_{z1} = 2$, $l_{x2} = l_{y2} = l_{z2} = 1.5$, $l_{x3} = l_{y3} = l_{z3} = 1.5$, and $L_x = L_y = L_z = 1$. The initial values of system states are taken as $x_0 = 170$ m, $y_0 = -20$ m, $z_0 = 180$ m, $\psi_0 = \pi/2$ rad, and $\gamma_0 = -\pi/4$ rad. The initial values of the path parameters are taken as $\theta_0 = 0$ rad and $\dot{\theta}_0 = 0.1$ rad/s. The sinusoidal wind gusts are considered in the simulation as $w_x = 2\sin(0.1t)$ m/s, $w_y = 2\sin(0.1t)$ m/s, and $w_z = 0.5\sin(0.1t) + 1$ m/s. To evaluate the influence of the prediction horizon on the path-following performance,

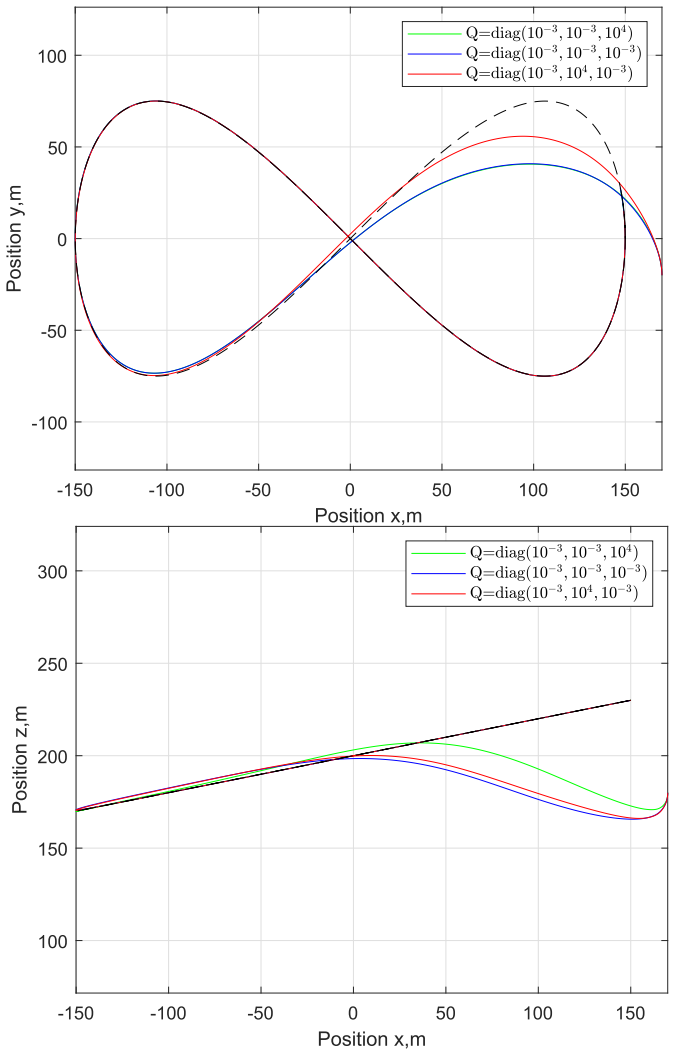

Fig. 3. Position profiles of a "bow-tie"-shaped path-following simulation for the fixed-wing UAV in the presence of wind gusts under different weighting matrices Q.

three different prediction horizons $T_P = 15$, 20, and 25 s have been tested in the simulation studies.

The simulations are performed based on the UAV kinematics model. The 3-D position profile for the path-following response is shown in Fig. 1. The corresponding control inputs are plotted in Fig. 2.

It can be observed from Fig. 1 that the proposed path-following algorithm can achieve offset-free following results for the given 3-D geometric path even in the presence of time-varying wind disturbances. It is also shown in Fig. 1 that the prediction horizon has a close impact on the convergence rate of the path-following errors. As shown in Fig. 1, the smaller prediction horizon T_P will result in faster convergence of the path-following errors. However, it can also be observed from Fig. 2 that the smaller T_P also leads to slightly more aggressive roll and flight path angle commands. As such, when tuning the predictive controllers proposed in this article, we should consider the tradeoff between the performance specification for path following and attitude constraints. Nevertheless, in practice, the convergence rate of the path-following algorithm can be effectively adjusted by tuning the parameter T_P.

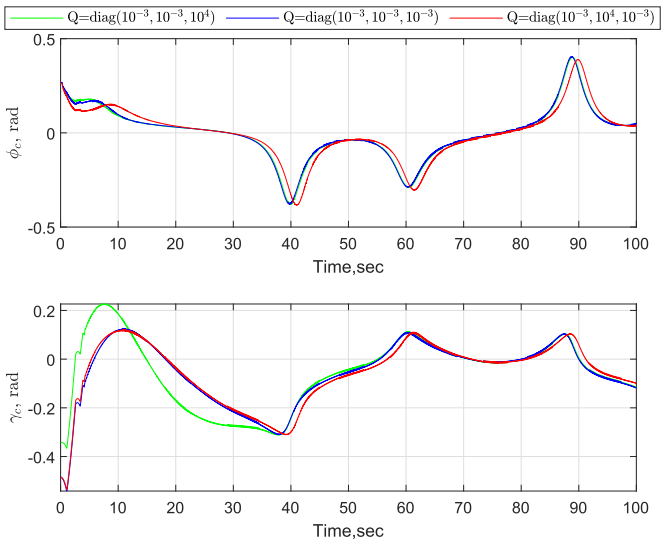

Fig. 4. Corresponding control inputs of a "bow-tie"-shaped path-following simulation under different weighting matrices Q.

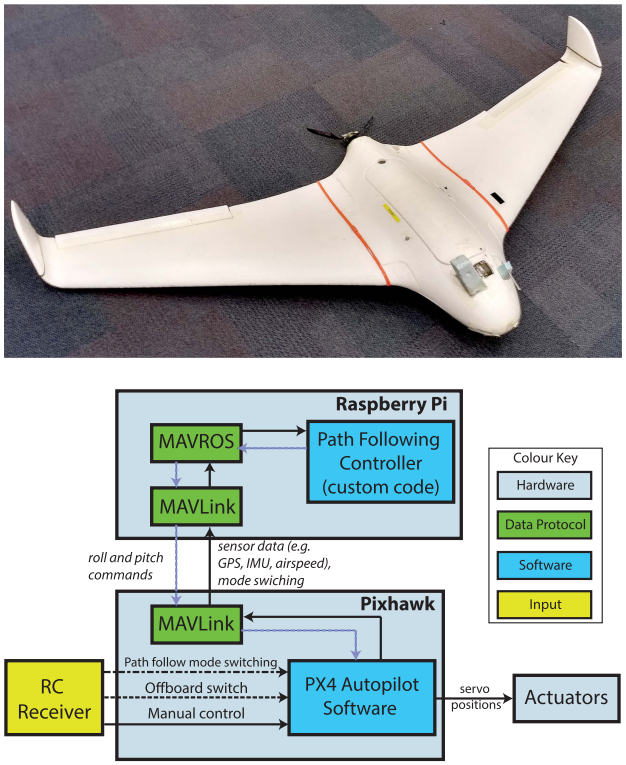

Fig. 5. Top: Skywalker X8 fixed-wing UAV used for flight test. Bottom: hardware configuration of the flight test platform.

B. Discussion on the Effects of Control Parameters

In the presence of the terminal cost, the relation between the weighting matrices P and Q can be used to adjust the convergence rate of different outputs. In this case study, the controller parameters are chosen as $r = 0$, $P = I_{3\times3}$, and $T_p = 10$, whereas the observer parameters, initial conditions, and wind gusts are all chosen the same as those in the previous study. To evaluate the influence of the weighting matrix on path-following performance, three different weighting matrices $Q = 10^{-3}\text{diag}(1, 1, 10^7)$, $10^{-3}\text{diag}(1, 1, 1)$, and

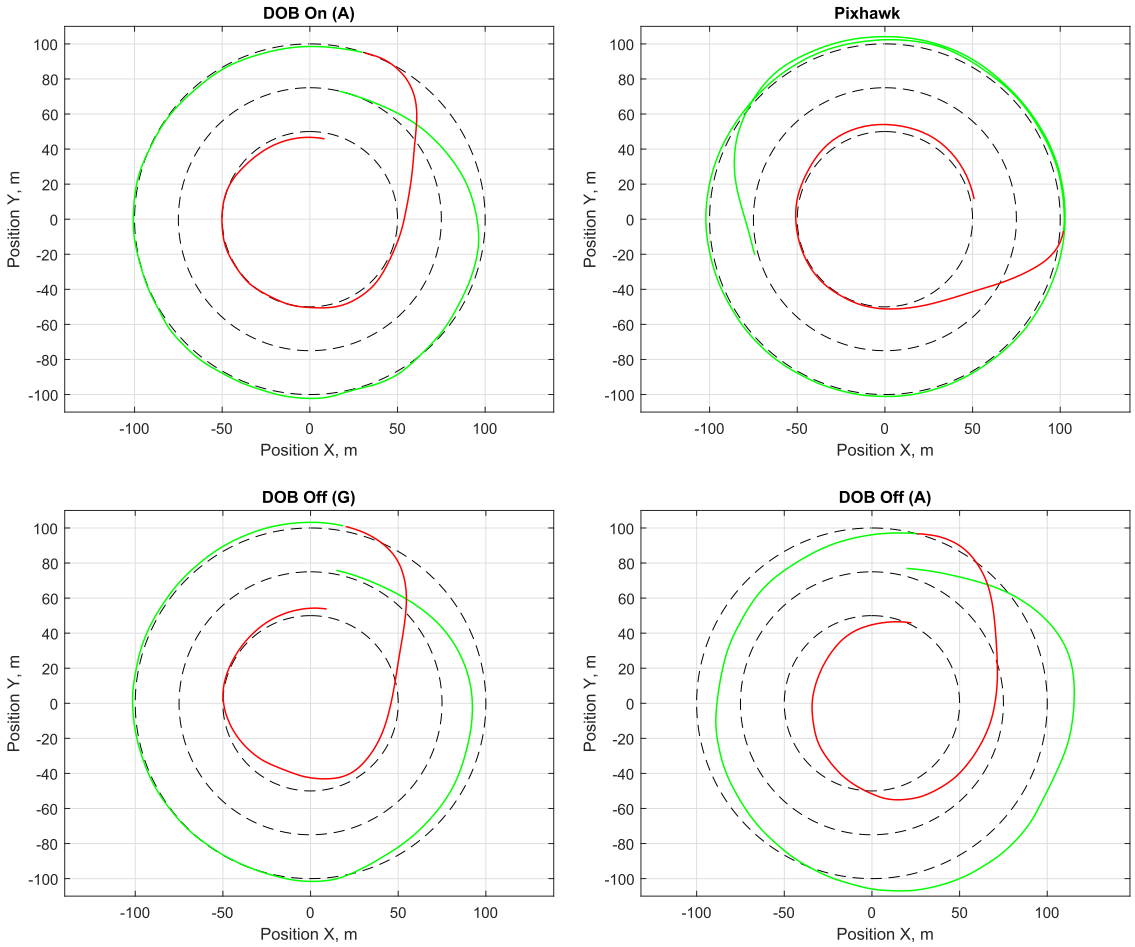

Fig. 6. Transition path-following profile of the fixed-wing UAV in the presence of wind gusts under the four guidance algorithms. The reference radius is changed from 75 to 100 m (Transition I) and, thereafter, from 100 to 50 m (Transition II).

$10^{-3}\text{diag}(1, 10^7, 1)$ have been tested in the simulation studies. To clearly demonstrate the convergence rate along different directions, the 2-D position profiles are shown in Fig. 3. The corresponding control inputs are plotted in Fig. 4.

It can be observed from Fig. 3 that by tuning the weighting matrix Q, the convergence rates of the path-following errors along x-, y-, and z-axes can be tuned separately, providing more freedom to achieve better performance in practice.

VI. Onboard Flight Experiment

To demonstrate the performance of the proposed path-following solution, thorough and fair flight tests have been conducted on a small UAV platform. In addition to testing different settings of the proposed algorithm, we also directly compared it with the path-following function available on the Pixhawk autopilot [33], which is arguably the most widely used commercial-off-the-shelf autopilot. Its guidance algorithm is designed based on the popular L_1 guidance law [14], [34]. The UAV platform, flight test procedures, and results are detailed in this section.

A. Flight Test Platform

A Skywalker X-8 fixed-wing aircraft is used in this article as the flight test platform. It is a popularly small UAV airframe that has been used in several research projects (see [35], [36]). The aircraft is equipped with a Pixhawk autopilot managing all aspects of the aircraft during the tests. A secondary flight computer based on Raspberry Pi2 is also installed on the aircraft and integrated with the Pixhawk. The X-8 aircraft and onboard electronics configuration is shown in Fig. 5.

In the flight test, the Pixhark autopilot is used as an inner loop controller to stabilize the aircraft and to follow the guidance commands sent from the Raspberry Pi2 flight computer, where the proposed algorithm is implemented. Due to that flight path angle control that is not available on this low-cost autopilot, the pitch angle command is used for the height control instead of γ_c, on the assumption that the angle of attack is small. The integration between the path following and the low-level control is achieved by intercepting the autopilot telemetry from the Raspberry Pi2 running the Robotic Operating System (ROS). Using an ROS package called MAVROS allows all the autopilot telemetry data to be added to the ROS network as topics, which then can be subscribed by other programs, including the custom path-following code on the Raspberry Pi2.

To enable rapid prototyping, the developed algorithm is constructed in the MATLAB/Simulink environment and then compiled into the C/C++ code using the MATLAB Embedded Coder. For flight tests, the resulted implementable code is

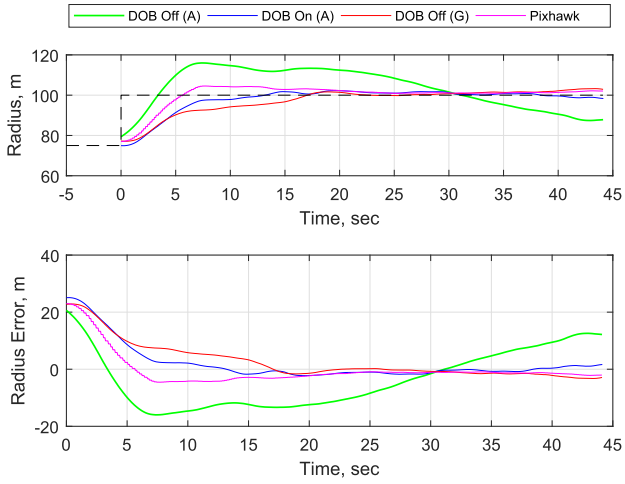

Fig. 7. Transition path-following radius (top) and radius error (bottom) of the fixed-wing UAV in the presence of wind gusts under the four guidance algorithms. The reference radius is changed from 75 to 100 m (Transition I).

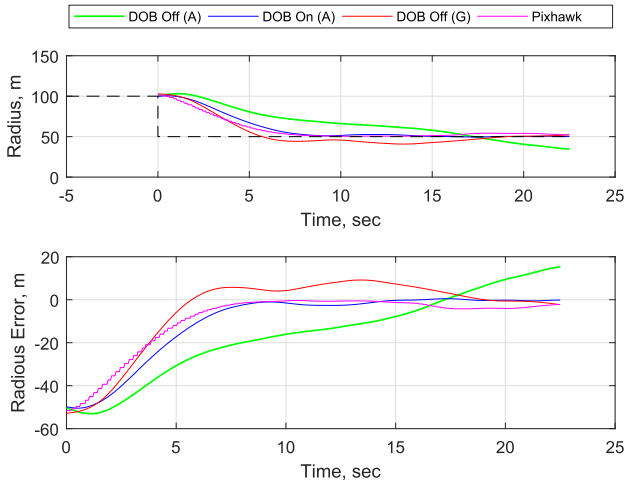

Fig. 8. Transition path-following radius (top) and radius error (bottom) of the fixed-wing UAV in the presence of wind gusts under the four guidance algorithms. The reference radius is changed from 100 to 50 m (Transition II).

directly deployed onto the Raspberry Pi2 running at 25 Hz. This also helps to reduce the latency when communicating with the Pixhawk autopilot.

B. Flight Test Procedure

To demonstrate the performance of the proposed algorithm, four different path-following functions were implemented and tested on the X-8 platform in sequence. First, the guidance algorithm on Pixhawk was tested as a default path-following function because it is well accepted by the user community. Second, the optimal path-following algorithm using ground speed and course was carried out since this is a common method for wind gust attenuation. Next, the same algorithm but using airspeed and heading angle was tested to demonstrate the influence of wind disturbance clearly. Finally, the proposed optimal path-following algorithm augmented with disturbance observer was performed. The abovementioned four algorithms are denoted as Pixhawk, DOB-Off (G), DOB-Off (A), and DOB-On (A), respectively, to facilitate the following discussion. It should be noted that for the Pixhawk guidance algorithm, an extended Kalman filter is used to fuse GPS velocities, airspeed, and compass heading to estimate the ground speed vector rather than using the GPS velocity directly.

Since the default guidance algorithm in Pixhawk only works for 2-D cases, we tested all four algorithms in a planer flight pattern to enable a direct comparison. Based on the simulation study, the control parameters of the proposed algorithm are chosen as $r = 1$, $T_P = 20$, $P = 0_{3\times3}$, and $Q = I_{3\times3}$ for the flight tests. This avoids a high-gain controller and presents a mild convergence of the path-following error. Moreover, the parameters of wind observers are selected as $l_{x1} = l_{y1} = l_{z1} = 2$, $l_{x2} = l_{y2} = l_{z2} = 1.5$, $l_{x3} = l_{y3} = l_{z3} = 1.5$, and $L_x = L_y = L_z = 1$. As a rule of thumb, the observer dynamics can be set 2–3 times faster than that of the control loop. It should be noted that the observer gains can be further tuned in experiments to trade off between the convergence rate and the attenuation of sensor noises.

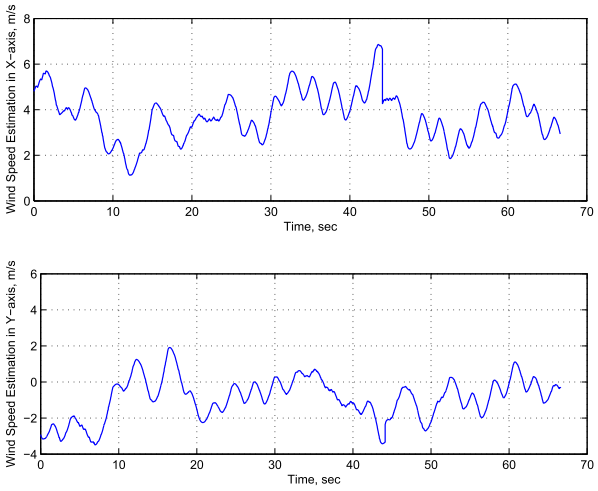

Fig. 9. Wind gust estimation for the transition case of flight test.

It is well known that different weather conditions may cause variations on the flight test results, especially for small UAV platforms. To minimize this influence and provide a fair comparison among different algorithms, we conducted the flight tests for four algorithms in one sortie within 15 min. During this short period, the weather condition was very consistent. In the flight tests, the algorithms were switched ON in sequence to follow the same reference path. The reference path consists of three circles with different radius to assess both transient responses and the disturbance compensation capability. The performance index of the integral of absolute error (IAE) is utilized to qualitatively evaluate the path-following performance specification of the four algorithms.

C. Transition Performance Comparison

For transition performance test and comparison, the radius of the reference geometric path is supposed to change from 75 to 100 m (denoted as Transition I) first and then reduce from 100 to 50 m (denoted as Transition II). The transition planer path-following profiles under the four different algorithms are shown in Fig. 6. The corresponding radius step responses as

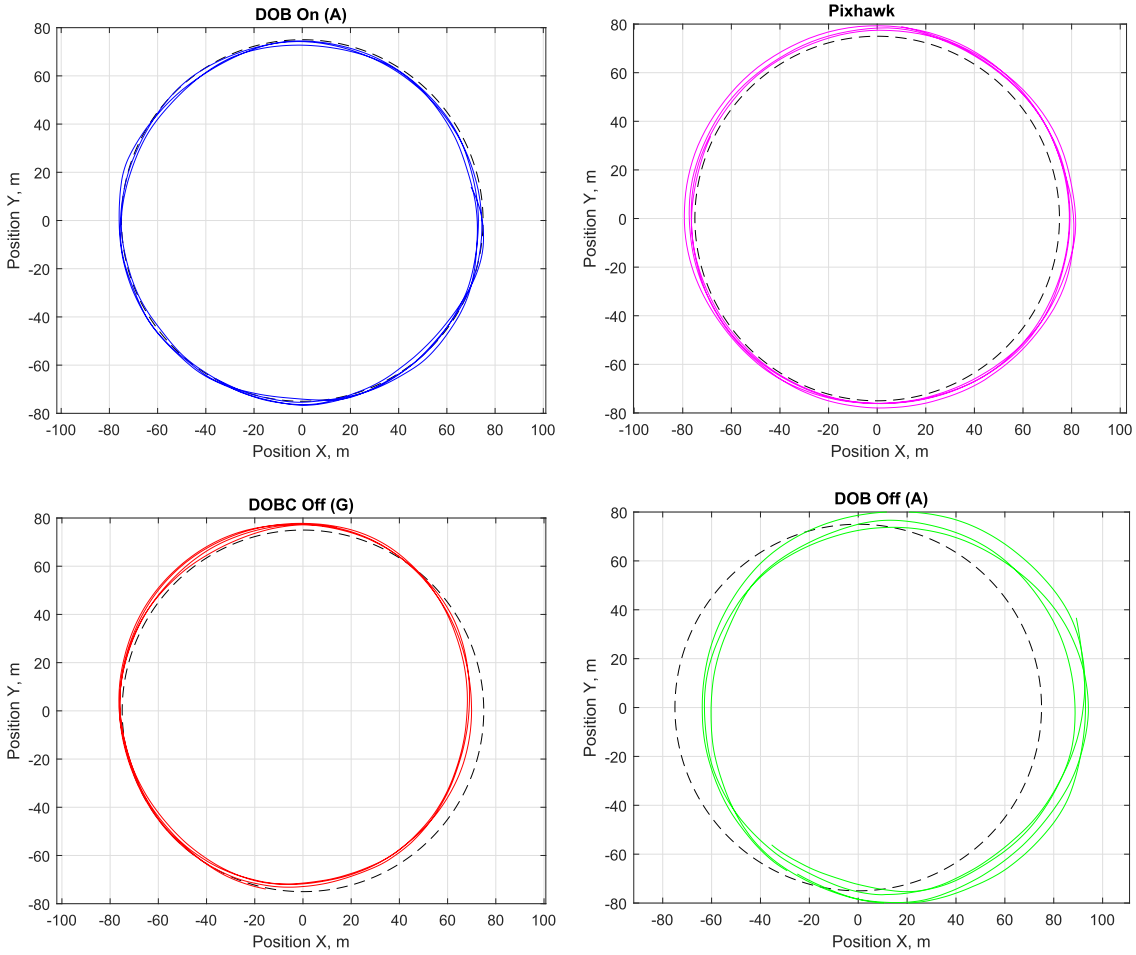

Fig. 10. Steady-state path-following profile of the fixed-wing UAV in the presence of wind gusts under the four guidance algorithms. The reference radius is 75 m (steady-state case).

TABLE I
PERFORMANCE INDEX OF IAE FOR THE FOUR PATH-FOLLOWING ALGORITHMS

Algorithms	Transition I (m)	Transition II (m)	Steady-State (m)
DOB On (A)	147.5	230.0	117.1
Pixhawk	152.9	207.3	364.4
DOB Off (G)	186.4	248.8	303.8
DOB Off (A)	423.1	453.2	1153.4

well as radius errors of two piecewise constant path-following tasks are shown in Figs. 7 and 8, respectively. The corresponding wind estimates for the transition process are given in Fig. 9, which shows an average wind magnitude of 4.0 m/s with a standard deviation of 1.2 m/s. Although this average wind speed may not seem to be a large value, it actually counts for 30% of the aircraft airspeed during the flight test, thus having a significant impact on flight performance.

It can be observed from Figs. 6–8 that the DOB-Off (A) algorithm leads to large transient path-following error due to the presence of wind gusts. By utilizing the groundspeed and course angle, the DOB-Off (G) algorithm has achieved much better transient performance compared with the DOB-Off (A) one. However, it shows some sluggish responses in Fig. 7 and small overshoot in Fig. 8. Moreover, the performance index of IAE for both Transitions I and II are given in Table I. It can be noted from Table I that the default Pixhawk guidance

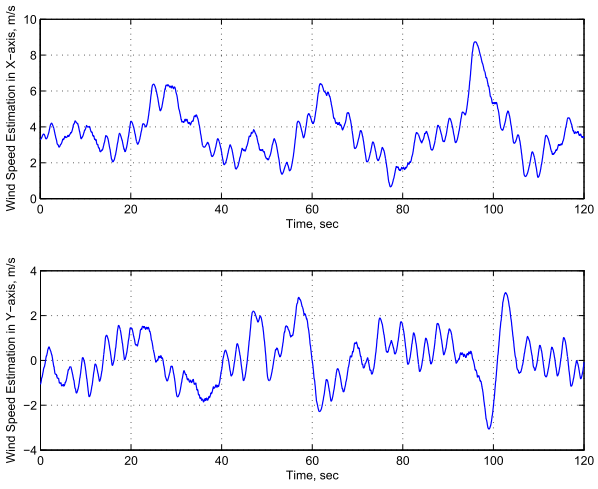

Fig. 11. Wind gust estimation for the steady-state case of flight test.

algorithm has achieved prominent transition performance. The proposed DOB-On (A) algorithm exhibits a comparable, if not better, transient performance compared with the L_1 guidance algorithm. It has smaller overshoot in Fig. 7 but shows slightly slow response in Fig. 8, albeit a similar settling time. This, however, confirms that a set of gentle control gains were selected in the proposed path-following algorithm, which would not make an extra contribution to disturbance rejection.

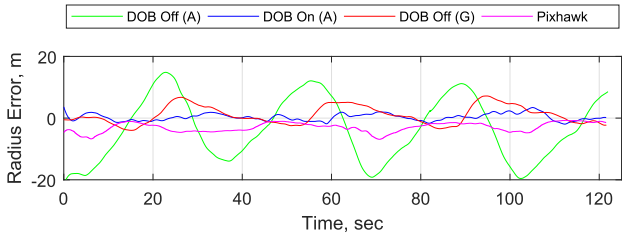

Fig. 12. Steady-state path-following radius error of the fixed-wing UAV in the presence of wind gusts under the four guidance algorithms (steady-state case).

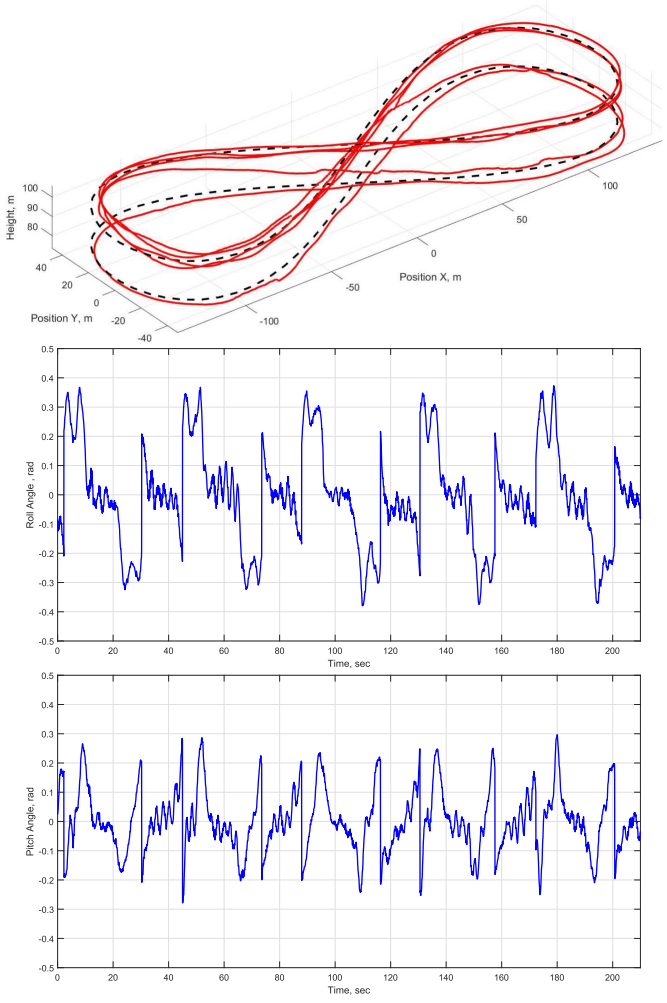

Fig. 13. 3-D position profile of a "bow-tie"-shaped path following (outdoor flight test result).

D. Steady-State Performance Comparison

In this section, we intend to verify the steady-state path-following performance of the proposed algorithm. The orbit radius of the desired path is 75 m, and each algorithm has been asked to follow this reference for at least 120 s to guarantee the consistency of the results. The steady-state planer path-following profiles of the four algorithms are shown in Fig. 10. The wind gust estimations by the nonlinear observers for the steady-state case are presented in Fig. 11. The average wind magnitude for this case is 3.8 m/s with a standard deviation of 1.4 m/s, which is consistent with wind estimates in Fig. 9. The corresponding steady-state radius errors of steady-state path-following profiles are shown in Fig. 12. The IAE performance

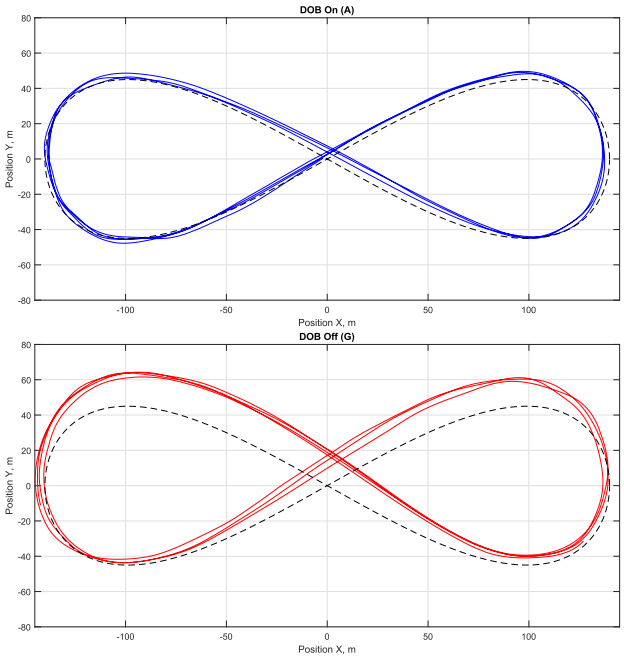

Fig. 14. 2-D position profile of a "bow-tie"-shaped path following (outdoor flight test result).

index in steady state is also calculated and shown in Table I for all the four path-following algorithms.

Again, it can be observed from Figs. 10 and 12 that the baseline approach DOB-Off (A) exhibits a large steady-state path-following error due to the existence of wind gusts. The Pixhawk and DOB-Off (G) algorithms significantly improve the steady-state path-following performance. However, there still exhibit considerable steady-state path-following errors, as shown in Figs. 10 and 12. It can be observed from Figs. 10 and 12 that the proposed path-following algorithm has provided a substantial improvement on steady-state path-following performance compared with the other three ones. Specifically, it can be observed from Table I that the steady-state path-following error of the proposed DOB On (A) method is about one-third of these of Pixhawk and DOB Off (G) algorithms.

E. "Bow-Tie"-Shaped Path-Following Flight Test

To demonstrate the ability of following more complex curves, additional flight tests were carried out on a "bow-tie"-shape reference path.[1] The planar path profile of the references is expressed as $x_d(\theta) = 140\cos(\theta)$ and $y_d(\theta) = 45\sin(2\theta)$, while the altitude $z_d(\theta)$ steps between 80 and 100 m during the transition process. The controller parameters adopt the same setting as in the previous flight tests. The flight test results on the 3-D "bow-tie"-shaped path-following profile, the corresponding roll angle, and pitch angle are given in Fig. 13.

Moreover, the flight test result on the 2-D "bow-tie"-shaped path following is given in Fig. 14, including the comparison results with ground speed-based path-following algorithm.

It can be seen from the flight test results given in Figs. 13 and 14 that the proposed path-following algorithm works well for more complex shapes such as 2-D and 3-D

[1]Video available at https://www.youtube.com/watch?v=M_qy1iH7u3M

"bow-tie" shapes. Also shown in Fig. 14, the proposed path-following algorithm outperforms the DOB Off (G) approach. This is the same as the conclusion obtained by circle path following in Sections VI-C and VI-D, except that the path-following error of DOB Off (G) increased significantly due to the tight turns making the ground velocity and course angle reading degraded.

VII. Conclusion

In this article, an optimal offset-free path-following algorithm has been proposed for generic fixed-wing UAVs without resorting to any geometric transformations. The nonlinear disturbance observers have been developed for environmental wind estimation and compensation. A major merit of the presented approach lies in that it is suitable for more general geometric path following rather than limited curvature such as straight line and circular orbit. The algorithm is simple and lightweight for online implementation and features effective gain tuning procedure and thus can be easily deployed on low-cost autopilots to improve the path-following capability of small UAVs. Experimental flight tests with various performance comparisons have been carried out on a fixed-wing UAV to validate the feasibility and effectiveness of the proposed algorithm. The flight test procedure and results are also complementary to the literature and thus can inform wider engineering practice in this area in terms of more effective exploitation of airspeed and magnetic heading in the flight control algorithm.

Appendix

The details of the proposed path-following algorithm are calculated here for the convenience of the readers. To begin with, the matrix $A(x)$ is calculated and given by

$$A(x) = \begin{bmatrix} -V\sin\psi\cos\gamma & -V\cos\psi\sin\gamma & -\nabla_\theta(x_d) \\ V\cos\psi\cos\gamma & -V\sin\psi\sin\gamma & -\nabla_\theta(y_d) \\ 0 & V\cos\gamma & -\nabla_\theta(z_d) \end{bmatrix}.$$

The proposed path-following guidance law is derived and provided as follows:

$$\begin{aligned}
\omega = {} & [(V\sin\psi\sin\gamma\,\nabla_\theta(z_d) + V\cos\gamma\,\nabla_\theta(y_d))v_x(x,\hat{d},\hat{a}) \\
& - (V\cos\gamma\,\nabla_\theta(x_d) + V\cos\psi\sin\gamma\,\nabla_\theta(z_d))v_y(x,\hat{d},\hat{a}) \\
& + (V\cos\psi\sin\gamma\,\nabla_\theta(y_d) - V\sin\psi\sin\gamma\,\nabla_\theta(x_d)) \\
& \times v_z(x,\hat{d},\hat{a})]/\Delta(x) \\
\nu = {} & [V\cos\psi\cos\gamma\,\nabla_\theta(z_d)v_x(x,\hat{d},\hat{a}) \\
& + V\sin\psi\cos\gamma\,\nabla_\theta(z_d)v_y(x,\hat{d},\hat{a}) \\
& - (V\cos\psi\cos\gamma\,\nabla_\theta(x_d) + V\sin\psi\cos\gamma\,\nabla_\theta(y_d)) \\
& \times v_z(x,\hat{d},\hat{a})]/\Delta(x) \\
\mu = {} & [(V^2\cos\psi\cos^2\gamma)v_x(x,\hat{d},\hat{a}) \\
& + (V^2\sin\psi\cos^2\gamma)v_y(x,\hat{d},\hat{a}) \\
& + (V^2\sin\gamma\,\cos\gamma)v_z(x,\hat{d},\hat{a})]/\Delta(x)
\end{aligned}$$

with

$$\begin{aligned}
\Delta(x) = {} & -V^2\sin\gamma\,\cos\gamma\,\nabla_\theta(z_d) \\
& -V^2\cos^2\gamma\,(\cos\psi\nabla_\theta(x_d) + \sin\psi\nabla_\theta(y_d)).
\end{aligned}$$

References

[1] R. W. Beard and T. W. McLain, *Small Unmanned Aircraft: Theory and Practical*. Princeton, NJ, USA: Princeton Univ. Press, 2012.

[2] G. Ambrosino, M. Ariola, U. Ciniglio, F. Corraro, E. De Lellis, and A. Pironti, "Path generation and tracking in 3-D for UAVs," *IEEE Trans. Control Syst. Technol.*, vol. 17, no. 4, pp. 980–988, Jul. 2009.

[3] E. W. Frew, D. A. Lawrence, and S. Morris, "Coordinated standoff tracking of moving targets using Lyapunov guidance vector fields," *J. Guid., Control, Dyn.*, vol. 31, no. 2, pp. 290–306, Mar. 2008.

[4] T. Oliveira, A. P. Aguiar, and P. Encarnacao, "Moving path following for unmanned aerial vehicles with applications to single and multiple target tracking problems," *IEEE Trans. Robot.*, vol. 32, no. 5, pp. 1062–1078, Oct. 2016.

[5] A. P. Aguiar, J. P. Hespanha, and P. V. Kokotovic, "Path-following for nonminimum phase systems removes performance limitations," *IEEE Trans. Autom. Control*, vol. 50, no. 2, pp. 234–239, Feb. 2005.

[6] A. P. Aguiar and J. P. Hespanha, "Trajectory-tracking and path-following of underactuated autonomous vehicles with parametric modeling uncertainty," *IEEE Trans. Autom. Control*, vol. 52, no. 8, pp. 1362–1379, Aug. 2007.

[7] A. P. Aguiar, J. P. Hespanha, and P. V. Kokotović, "Performance limitations in reference tracking and path following for nonlinear systems," *Automatica*, vol. 44, no. 3, pp. 598–610, Mar. 2008.

[8] R. W. Beard, J. Ferrin, and J. Humpherys, "Fixed wing UAV path following in wind with input constraints," *IEEE Trans. Control Syst. Technol.*, vol. 22, no. 6, pp. 2103–2117, Nov. 2014.

[9] P. B. Sujit, S. Saripalli, and J. B. Sousa, "Unmanned aerial vehicle path following: A survey and analysis of algorithms for fixed-wing unmanned aerial vehicles," *IEEE Control Syst.*, vol. 34, no. 1, pp. 42–59, Feb. 2014.

[10] D. R. Nelson, D. B. Barber, T. W. McLain, and R. W. Beard, "Vector field path following for miniature air vehicles," *IEEE Trans. Robot.*, vol. 23, no. 3, pp. 519–529, Jun. 2007.

[11] D. A. Lawrence, E. W. Frew, and W. J. Pisano, "Lyapunov vector fields for autonomous unmanned aircraft flight control," *J. Guid., Control, Dyn.*, vol. 31, no. 5, pp. 1220–1229, Sep. 2008.

[12] H. Chen, K. Chang, and C. S. Agate, "UAV path planning with Tangent-plus-Lyapunov vector field guidance and obstacle avoidance," *IEEE Trans. Aerosp. Electron. Syst.*, vol. 49, no. 2, pp. 840–856, Apr. 2013.

[13] E. W. Frew and D. Lawrence, "Tracking dynamic star curves using guidance vector fields," *J. Guid., Control, Dyn.*, vol. 40, no. 6, pp. 1488–1495, Jun. 2017.

[14] S. Park, J. Deyst, and J. P. How, "Performance and Lyapunov stability of a nonlinear path following guidance method," *J. Guid., Control, Dyn.*, vol. 30, no. 6, pp. 1718–1728, Nov. 2007.

[15] I. Kaminer, A. Pascoal, E. Xargay, N. Hovakimyan, C. Cao, and V. Dobrokhodov, "Path following for small unmanned aerial vehicles using L1 adaptive augmentation of commercial autopilots," *J. Guid., Control, Dyn.*, vol. 33, no. 2, pp. 550–564, Mar. 2010.

[16] R. Rysdyk, "Unmanned aerial vehicle path following for target observation in wind," *J. Guid., Control, Dyn.*, vol. 29, no. 5, pp. 1092–1100, Sep. 2006.

[17] C. Liu, O. McAree, and W.-H. Chen, "Path-following control for small fixed-wing unmanned aerial vehicles under wind disturbances," *Int. J. Robust Nonlinear Control*, vol. 23, no. 15, pp. 1682–1698, 2013.

[18] E. Xargay *et al.*, "Time-critical cooperative path following of multiple unmanned aerial vehicles over time-varying networks," *J. Guid., Control, Dyn.*, vol. 36, no. 2, pp. 499–516, Mar. 2013.

[19] N. Cho, Y. Kim, and S. Park, "Three-dimensional nonlinear differential geometric path-following guidance law," *J. Guid., Control, Dyn.*, vol. 38, no. 12, pp. 2366–2385, Dec. 2015.

[20] L. Furieri, T. Stastny, L. Marconi, R. Siegwart, and I. Gilitschenski, "Gone with the wind: Nonlinear guidance for small fixed-wing aircraft in arbitrarily strong windfields," in *Proc. Amer. Control Conf. (ACC)*, May 2017, pp. 4254–4261.

[21] F. Gavilan, R. Vazquez, and E. F. Camacho, "An iterative model predictive control algorithm for UAV guidance," *IEEE Trans. Aerosp. Electron. Syst.*, vol. 51, no. 3, pp. 2406–2419, Jul. 2015.

[22] A. Rucco, A. P. Aguiar, F. L. Pereira, and J. B. de Sousa, "A predictive path-following approach for fixed-wing unmanned aerial vehicles in presence of wind disturbances," in *Proc. Robot 2nd Iberian Robot. Conf.* Cham, Switzerland: Springer, 2016, pp. 623–634.

[23] A. Alessandretti and A. P. Aguiar, "A planar path-following model predictive controller for fixed-wing unmanned aerial vehicles," in *Proc. 11th Int. Workshop Robot Motion Control (RoMoCo)*, Jul. 2017, pp. 59–64.

[24] T. Faulwasser and R. Findeisen, "Nonlinear model predictive control for constrained output path following," *IEEE Trans. Autom. Control*, vol. 61, no. 4, pp. 1026–1039, Apr. 2016.
[25] A. Brezoescu, T. Espinoza, P. Castillo, and R. Lozano, "Adaptive trajectory following for a fixed-wing UAV in presence of crosswind," *J. Intell. Robotic Syst.*, vol. 69, nos. 1–4, pp. 257–271, Jan. 2013.
[26] J. Yang, C. Liu, Z. Zuo, and W.-H. Chen, "A simple optimal planer path following algorithm for unmanned aerial vehicles," in *Proc. Eur. Control Conf. (ECC)*, Jun. 2018, pp. 1809–1814.
[27] W.-H. Chen, D. J. Ballance, and P. J. Gawthrop, "Optimal control of nonlinear systems: A predictive control approach," *Automatica*, vol. 39, no. 4, pp. 633–641, Apr. 2003.
[28] A. Isidori, *Nonlinear Control Systems*. London, U.K.: Springer-Verlag, 2013.
[29] Y. Shtessel, C. Edwards, L. Fridman, and A. Levant, *Sliding Mode Control and Observation*. New York, NY, USA: Springer, 2014.
[30] W.-H. Chen, "Disturbance observer based control for nonlinear systems," *IEEE/ASME Trans. Mechatronics*, vol. 9, no. 4, pp. 706–710, Dec. 2004.
[31] C. Zhang, Y. Yan, C. Wen, J. Yang, and H. Yu, "A nonsmooth composite control design framework for nonlinear systems with mismatched disturbances: Algorithms and experimental tests," *IEEE Trans. Ind. Electron.*, vol. 65, no. 11, pp. 8828–8839, Nov. 2018.
[32] H. K. Khalil, *Noninear Systems*. Upper Saddle River, NJ, USA: Prentice-Hall, 1996.
[33] *Navigation Tuning With the L1 Controller*. Accessed: Apr. 15, 2018. [Online]. Available: http://ardupilot.org/plane/docs/navigation-tuning.html
[34] S. Park, J. Deyst, and J. How, "A new nonlinear guidance logic for trajectory tracking," in *Proc. AIAA Guid., Navigat., Control Conf. Exhibit*, Aug. 2004, pp. 1–16.
[35] T. A. Johansen, A. Cristofaro, K. Sorensen, J. M. Hansen, and T. I. Fossen, "On estimation of wind velocity, angle-of-attack and sideslip angle of small UAVs using standard sensors," in *Proc. Int. Conf. Unmanned Aircr. Syst. (ICUAS)*, Jun. 2015, pp. 510–519.
[36] R. Skulstad, C. Syversen, M. Merz, N. Sokolova, T. Fossen, and T. Johansen, "Autonomous net recovery of fixed-wing UAV with single-frequency carrier-phase differential GNSS," *IEEE Aerosp. Electron. Syst. Mag.*, vol. 30, no. 5, pp. 18–27, May 2015.

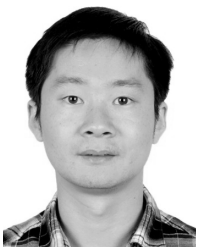

Jun Yang (Senior Member, IEEE) received the B.Sc. degree from the Department of Automatic Control, Northeastern University, Shenyang, China, in 2006, and the Ph.D. degree in control theory and control engineering from the School of Automation, Southeast University, Nanjing, China, in 2011.

He is currently a Professor with the School of Automation, Southeast University. His current research interests include disturbance estimation and compensation, advanced control theory, and its application to flight control systems and motion control systems.

Dr. Yang received the Premium Award for best paper for *IET Control Theory and Applications* in 2017 and the ICI Prize for best paper of the *Transactions of the Institute of Measurement and Control* in 2016. He is an Associate Editor of the *Transactions of the Institute of Measurement and Control*.

Cunjia Liu (Member, IEEE) received the B.Eng. and M.Sc. degrees in guidance, navigation, and control from Beihang University, Beijing, China, in 2005 and 2008, respectively, and the Ph.D. degree in autonomous vehicle control from Loughborough University, Loughborough, U.K., in 2011.

He was a Research Associate with the Department of Aeronautical and Automotive Engineering, Loughborough University, where he was appointed as a Lecturer and then a Senior Lecturer in unmanned vehicles in 2013 and 2018, respectively. His current research interests include advanced control, Bayesian estimation, autonomous systems and their applications in aerospace, and automotive and agriculture domains.

Matthew Coombes received the M.Eng. degree in aeronautical engineering and the Ph.D. degree in autonomous vehicles from the Department of Aeronautical and Automotive Engineering, Loughborough University, Loughborough, U.K., in 2010 and 2015, respectively.

He is currently a Lecturer in autonomous vehicles with the Department of Aeronautical and Automotive Engineering, Loughborough University. He has considerable experience in developing and operating autonomous aerial platforms, including system and control design, sensor integration, and flight testing. His research spans across a number of areas related to autonomous vehicles. Some of them include unmanned aerial vehicle forced landing, situational awareness, and autonomous taxiing. His more recent work has been on mission planning optimization for agricultural aerial surveying.

Yunda Yan (Member, IEEE) received the B.Sc. degree in automation and the Ph.D. degree in control theory and control engineering from the School of Automation in Southeast University, Nanjing, China, in 2013 and 2019, respectively.

He was a Visiting Student with the Department of Biomedical Engineering, National University of Singapore, Singapore, in 2017. He was a Visiting Student with the Department of Aeronautical and Automotive Engineering, Loughborough University, Loughborough, U.K., in 2018, where he is currently a Research Associate. His research interests include the development of predictive control methods, control allocation methods, dynamic high-gain control methods, and disturbance modeling and estimation approaches and their applications in motion and flight control systems.

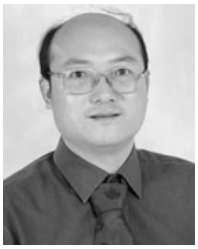

Wen-Hua Chen (Fellow, IEEE) received the M.Sc. and Ph.D. degrees from the Department of Automatic Control, Northeastern University, Shenyang, China, in 1989 and 1991, respectively.

From 1991 to 1996, he was a Lecturer with the Department of Automatic Control, Nanjing University of Aeronautics and Astronautics, Nanjing, China. He held a research position and then a lectureship in control engineering at the Centre for Systems and Control, University of Glasgow, Glasgow, U.K., from 1997 to 2000. He is currently a Professor in autonomous vehicles with the Department of Aeronautical and Automotive Engineering, Loughborough University, Loughborough, U.K. He has published three books and 250 papers in journals and conferences. His research interests include the development of advanced control strategies and their applications in aerospace engineering, particularly in unmanned aircraft systems.

Dr. Chen is a fellow of the Institution of Engineering and Technology and the Institution of Mechanical Engineers. He was a recipient of the prestigious EPSRC Established Career Fellowship Award.